Contents lists available at ScienceDirect

Chemical Engineering Research and Design

journal homepage: www.elsevier.com/locate/cherd

High-speed video investigation of jet dynamics from narrow orifices for needle-free injection

*M. Moradiafrapoli, J.O. Marston**

Department of Chemical Engineering, Texas Tech University, Lubbock, TX 79409, United States

ARTICLE INFO

Article history:
Received 20 June 2016
Received in revised form 15 September 2016
Accepted 13 October 2016
Available online 21 October 2016

Keywords:
Needle-free injection
Liquid jet
Hydrodynamics

ABSTRACT

An experimental study to examine the hydrodynamic performance and start-up phase of liquid jets for needle-free injection was performed. With the use of high-speed videography at frame rates up to 311,111 fps, the initial stages of jets exiting from narrow orifices were captured. In addition to the very early-time ($t < 50\,\mu s$) dynamics, we assessed the fully-developed jet form and the penetration dynamics into various gel substrates. The viscosity of the jet fluid was varied along with the nozzle diameter, and the gel stiffness (by varying the solids fraction, $\%_{w/w}$). For the penetration into gels, we observe that the speed of the tip of the hole did not exhibit any quantifiable dependence of jet fluid properties. Moreover, we observe the formation of fluid reservoirs which led to a step-wise penetration regime for depths $z \gtrsim 12\,mm$.

1. Introduction

Needle-free injection devices are becoming increasingly attractive as a means of depositing a liquid into sub-cutaneous or intramuscular regions, primarily for drug delivery and vaccination purposes. Some factors often cited for developing such devices are phobia of needles, needle-stick injuries, and contamination due to needle re-use (Mitragotri, 2006; Kale and Momin, 2014). The principle goal of needle-free injection devices is to achieve a precise deposition of drug without the use of a solid needle, by using a high-speed liquid jet (Schramm-Baxter and Mitragotri, 2004; Baxter and Mitragotri, 2005; Park et al., 2012; Kato et al., 2014; Flethcer et al., 2002). In addition to liquid jets, which can incorporate macromolecules (Michinaka and Mitragotri, 2011; Arora et al., 2007, 2008), particulate injection has also been investigated (Kendall et al., 2004a,b).

A primary determinant in the relatively limited use of needle-free injectors is cost, whereby traditional stainless steel needle tips are typically less than one fiftieth of the cost of a disposable tip used in needle-free injectors (Stout, 2016). However, given the cost associated with treatment of needle-stick injury and cross-contamination arising from needle re-use, and the potential for a host of different applications, it is clear that the field of needle-free drug delivery, especially techniques using jets, requires more research to expand upon the current restricted use.

The purpose of this study was to provide detailed high-speed visualization of the jet to better understand the salient features – namely – the early-time jet formation dynamics and jet penetration into target substrates.

1.1. *Current marketed technology*

Needle-free injectors have been in existence since the mid 1930s (Mitragotri, 2006) and were popularized by the US military for rapid vaccination of up to 1000 subjects per hour in the 1950's. However, development and refinement of the technology has suffered primarily due to issues of contamination between subjects when employing Multi-Use Nozzle Jet Injectors (MUNJIs). The focus thus shifted toward Disposable Cartridge Jet Injectors (DCJIs) for single-dose devices more suitable for home use.

* *Corresponding author.*
E-mail address: jeremy.marston@ttu.edu (J.O. Marston).
http://dx.doi.org/10.1016/j.cherd.2016.10.023

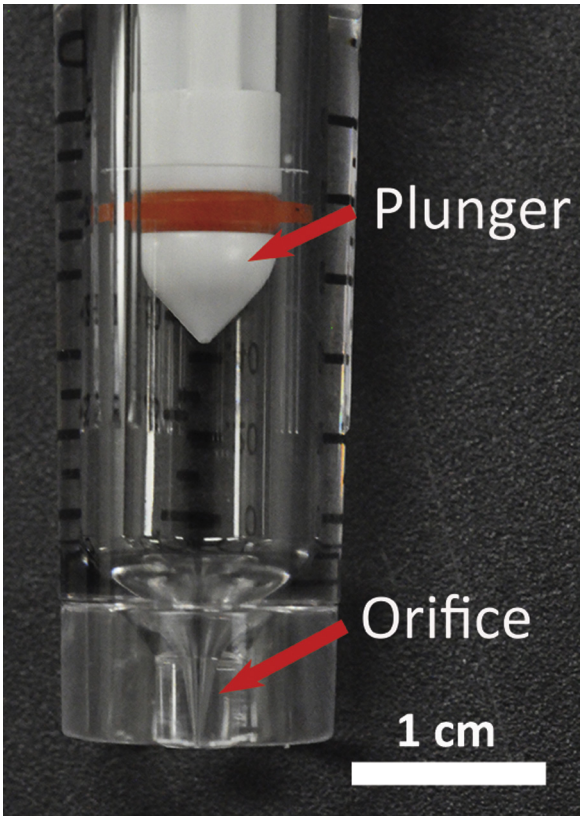

Fig. 1 – Disposable cartridge for plunger-actuated jets in needle-free injection.

Both types of injectors employ either a spring-loaded mechanism or a gas cartridge to actuate a plunger, an example of which is shown in Fig. 1. The actuation mechanism must provide sufficient and sustained injection pressure to achieve a steady, high-velocity jet. Furthermore, the principle relies upon the incompressible response of the liquid to the impulsive action of the plunger.

At present, several companies (e.g. Bioject, PharmaJet) have marketed products for a range of applications, however, the dynamics of the jets produced with such devices have not yet been well characterized and limitations in terms of jet fluid properties have not been explored. This observation provides significant motivation for the present study.

1.2. *Recent innovation*

Further to commercial technology employing springs and gas-powered actuators, designed primarily for single-injection and home-use, only a handful of studies have considered alternative approaches. Amongst these are piezoelectric devices (Stachowiak et al., 2007, 2009), with which jet diameters ranging from 40–130 μm and velocities from 50–160 m/s were observed for injection volumes of the order of 10 μL. Lorentz force actuators (Taberner et al., 2012) have also been used to achieve variable jet speeds up to ≈180 m/s with diameters of 220 μm and total injection volumes up to 250 μL. One potentially attractive feature of these two approaches is the option for dynamic control of the jet velocity through an integrated feedback system.

Another recent development (Tagawa et al., 2012, 2013) in the art of jet injection stems from the well-established principle of laser-induced cavitation (Philipp and Lauterborn, 1998; Lindau and Lauterborn, 2003; Vogel et al., 2007; Shrestha et al., 2010; Musapelo and Murray, 2014; Zhu et al., 2010; Stolee and Vertes, 2013; Apitz and Vogel, 2005; Frenz et al., 1989; Pohl et al., 2014). In this process, the basic working principle is that a high-energy laser pulse is focused into a cylindrical tube containing liquid. The ensuing optical breakdown of focused light energy creates a cavitation bubble that rapidly expands, sending a shock wave through the liquid (Marston and Thoroddsen, 2015; Thoroddsen et al., 2009; Heijnen et al., 2009; Chen et al., 2013a,b; Zhiyuan et al., 2014; Darling et al., 2008; Gregorcic et al., 2013; Lindinger et al., 2004; Frenz et al., 1996), and ejects a jet from an open end. This process is shown schematically in Fig. 2. This technique is fundamentally different since the jet that emerges is narrower than the orifice, whereas the other technologies described above force liquid out of the orifice so that the initial jet diameter is prescribed by the orifice diameter. At present, the authors are unaware of any applications of this jet formation technique to needle-free injections, although laser-induced cavitation was exploited for single-cell puncture in a previous study (Li et al., 2013).

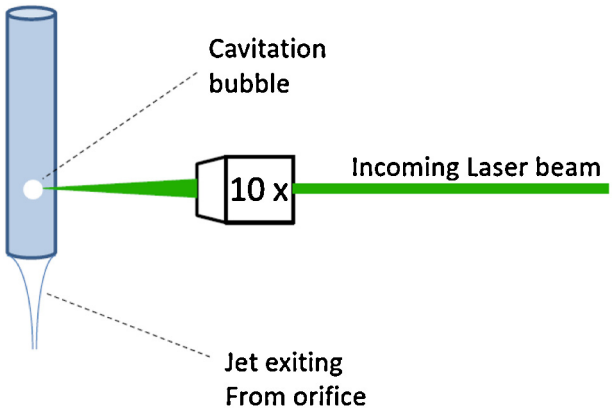

Fig. 2 – Schematic overview of laser-induced micro-jet formation.

Using this technique it is possible to dispense small volumes of liquid in the form of a truly slender jet with high precision, whereby the characteristics of the jet in terms of diameter and velocity can be fine-tuned. Therefore, an extended parameter space compared to the commercial devices may be available. It is this novel approach that we employ herein, purely for a qualitative comparison of jet streams to those for commercial devices. However, the primary goal of this work is to provide an overview of the salient features of high-speed jets emerging with a fixed diameter from a narrow orifice.

2. Materials and methods

The experimental study employed two jet formation methods. The first consisted of a commercial device – namely – the Biojector 2000 (Bioject Inc., Portland, OR, USA). The Biojector 2000 employs a gas cartridge to actuate the plunger. This device can accommodate a range of disposable tips (e.g. Fig. 1) to produce jets of different diameters and velocities. The two orifices tested herein have mean diameters of $D_0 = 114\ \mu m \pm 4\ \mu m$ and $D_0 = 157\ \mu m \pm 5\ \mu m$.

A small optomechanical cage was constructed and mounted to an optical table to secure the devices for testing which enabled easy focus for the high-speed video. Initial tests were conducted in air to simply view the start-up phase of the jet, in which case a glass beaker was place below the orifice to collect the dispensed liquid, whilst secondary tests were

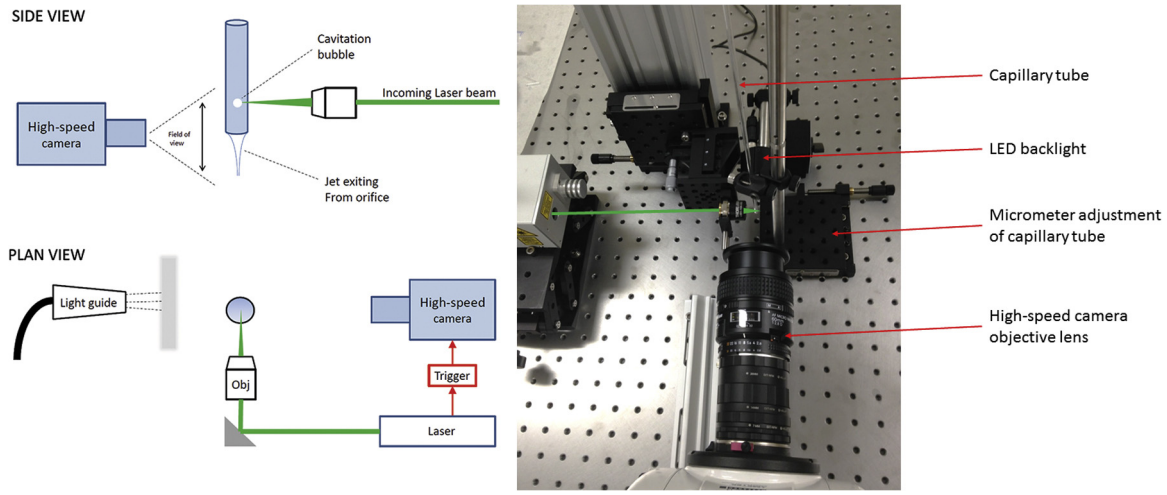

Fig. 3 – Schematic representations (left) and photograph (right) of the experimental setup for laser-induced jets.

conducted by placing a gel substrate a few millimeters below the orifice in order to observe the jet penetration dynamics.

The test fluids comprised pure water, 50% glycerol solution, 80% glycerol solution and 2% CMC solution (carboxymethyl cellulose). The viscosities of the water and water–glycerol mixtures are Newtonian with $\mu \approx 1$, 8, 85 mPa s, whilst the CMC solution is slightly shear-thinning, fitted best by the cross model:

$$\frac{\mu - \mu_\infty}{\mu_0 - \mu_\infty} = \frac{1}{1 + [\lambda\dot{\gamma}]^{(1-\alpha)}} \tag{1}$$

with $\mu_0 = 37$ mPa s, $\mu_\infty \approx 1$ mPa s, $\lambda = 1.2 \times 10^{-4}$ s and $\alpha = 0.03$. If we assume the velocity in the orifice is the same as the jet, $V_{jet} \sim O(100)$ m/s and the diameter of the orifice $D_0 \sim O(100)$ μm, then we can estimate the shear rate in the orifice as $\dot{\gamma} \sim V_{jet}/D_0 \approx 10^6\ s^{-1}$, giving viscosities as low as $\mu = 1.3$ mPa s, showing a significant reduction from $\mu_0 = 37$ mPa s.

The variation in density ($\rho = 1000$–$1210\ kg/m^3$) and surface tension ($\sigma = 67$–72 mN/m) was considered to be small compared to viscosity, therefore, the primary dimensionless parameter for characterizing the jet is the Reynolds number

$$Re_{jet} = \frac{\rho D_0 V_{jet}}{\mu} \tag{2}$$

where D_0 is the orifice diameter, and V_{jet} is the calculated jet speed. Based on our derivations of the fully-developed jet speed, we estimate the range of jet Reynolds numbers to be $Re_{jet} \approx 140$–$18{,}000$. For all the steady jet streams observed in the present study, the jet Weber number, $We_{jet} = \rho D_0 V_{jet}^2/\sigma = 3400$ up to 28,400. Despite this high Weber number regime, we did not observe jet instability as described by Gonzalez Avila et al. (2015), which occurred for $We_{jet} > 4600$. However, in some of the very earliest motions, very high Weber and Reynolds numbers are reached.

The events were captured with a high-speed video camera (V1611, Vision Research Inc.) at frames rates of up to 311,111 fps, giving minimum inter-frame times of 3.2 μs. The camera was equipped with a 60 mm micro-Nikkor lens and several extension tubes to render sufficient magnification to observe the small-scale features of the jet dynamics. The effective pixel size under typical magnification was below 50 μm/pixel. The video clips were auto-triggered using the built-in image trigger (IBAT) and saved to a PC for subsequent analysis. Uniform back-lighting was achieved using a micro-LED array and diffuser screen.

For the laser-induced jets, we employed an Nd:YAG pulsed laser (Nano-S 120-20, Litron Lasers Ltd., UK) with a maximum pulse energy of 120 mJ. Single pulses were focused to a spot size of approximately 50 μm through a high-powered objective lens into the center of a glass capillary tube with an inner diameter of up to 2.7 mm. A schematic of this setup is shown in Fig. 3.

3. Results and discussion

3.1. *Early jet dynamics and start-up phase*

The start of the jet in both the commercial devices and laser-induced method is extremely fast and reveals some rich dynamical features that would be missed completely without the high frame rates used herein. To highlight this, in Figs. 4–6 we present the reader with several sequences of the very first motions, typically occurring on the micro-second to millisecond time scale. The time taken to reach a steady stream is typically a few milliseconds, which is discussed in more detail later, thus we must probe the sub-millisecond timescale to capture these features.

In Fig. 4, we observe the early-time evolution of water exiting from a 157 μm-diameter orifice. The first frame in the sequence, labeled $t = 0$ is the frame immediately prior to the jet exit. The next three frames ($t = 9.6$–28.9 μs) show a slightly hazy appearance at the tip of the jet, which is assumed to be a fine cloud of sub-pixel-size droplets caused by atomization of the tip of the jet, which is to be expected in this very high-inertia regime ($Re = O(10^4)$, $We = O(10^5)$). Slight disturbances can be seen in the jet up until $t = 48.2$ μs, with a fuller jet appearing around $t = 318$ μs, although we still observe some spray around the main jet. At later times $t \gtrsim 900$ μs, the jet reaches a steady, stable configuration, as shown by the final image in the sequence.

The jet diameter at the bottom of the field-of-view (4.6 mm below the orifice) is 220 μm. Furthermore, based on the displacement over the first few frames from the jet emergence in Fig. 4, we estimate the initial exit speed to be $V_{exit} \approx 327$ m/s. Note that this is significantly higher than the steady-stream jet speed (see Section 3.3 for details) and likely caused by the impulse of the plunger immediately after actuation.

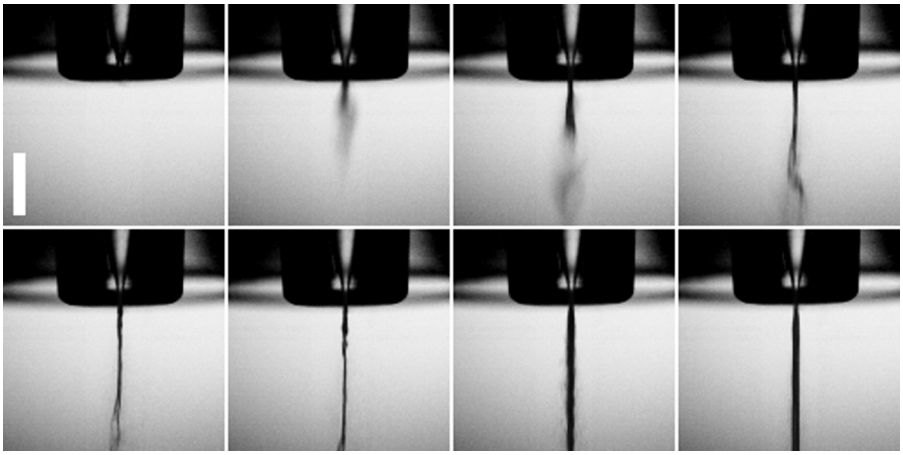

Fig. 4 – Frames from an high-speed video sequence taken at 311,111 fps of a water jet start-up phase for a gas actuated plunger device with an orifice diameter of 157 μm. The times from first detected motion of the jet are $t = 0$, 9.6, 19.3, 28.9, 38.6, 48.2, 318.2 and 3211 μs. The scale bar is 2 mm long.

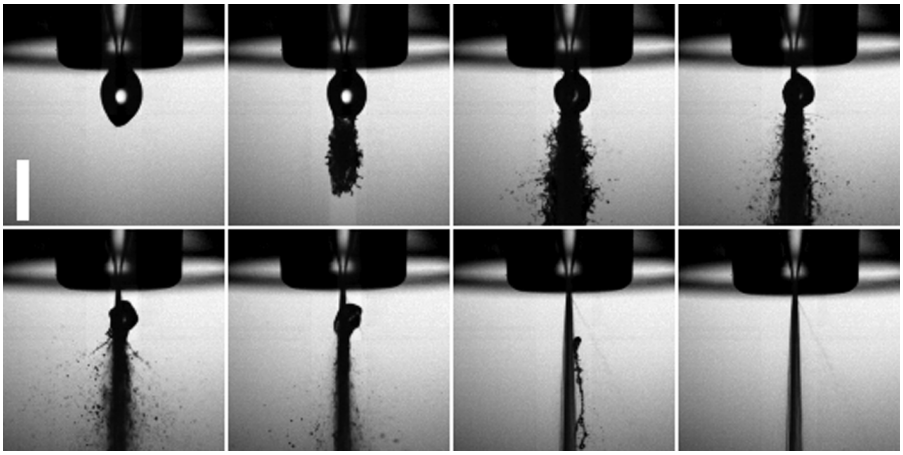

Fig. 5 – Frames from a high-speed video sequence taken at 311,111 fps of a water jet start-up phase for a gas actuated plunger device with an orifice diameter of 157 μm. In this instance, there is an existing defect (droplet) on the exterior of the nozzle orifice, causing a fine spray at for $t \lesssim 1$ ms. The times from first detected motion of the jet are $t = -3.2$, 125, 254, 511, 768, 1154, 3018 and 4111 μs. The scale bar is 2 mm long.

Fig. 5 shows another realization of water exiting from the same size orifice, whereby a droplet of water is present at the exit point just prior to the start of the plunger motion. The ensuing motion over the first few milliseconds shows a moderate delay in the jet start-up time as the initial droplet is dispelled through a spray of finer droplets. The steady jet formation (i.e. the final image in the sequence) in this case occurs at approximately 3.5 ms, where the approximate jet diameter

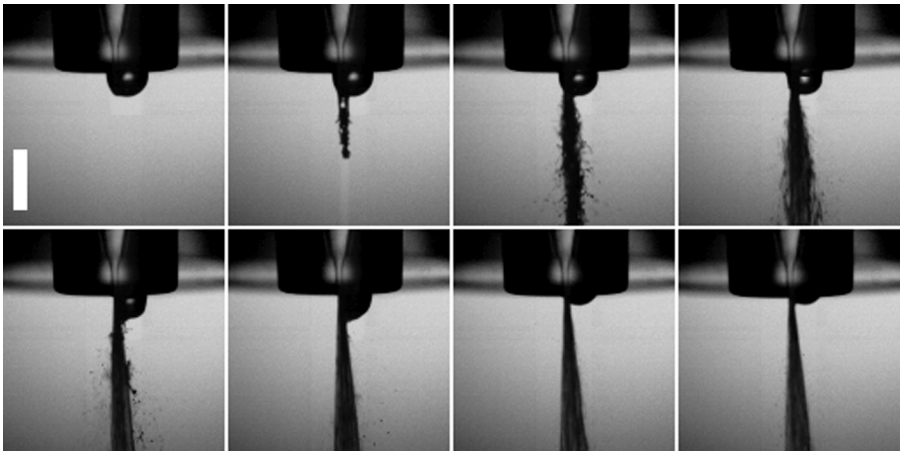

Fig. 6 – Frames from an ultra-high-speed video sequence taken at 311,111 fps of a 50% glycerol jet start-up phase for a gas actuated plunger device with an orifice diameter of 157 μm. The times from first detected motion of the jet are $t = -3.2$, 125, 254, 511, 768, 1154, 3018 and 4111 μs. The scale bar is 2 mm long.

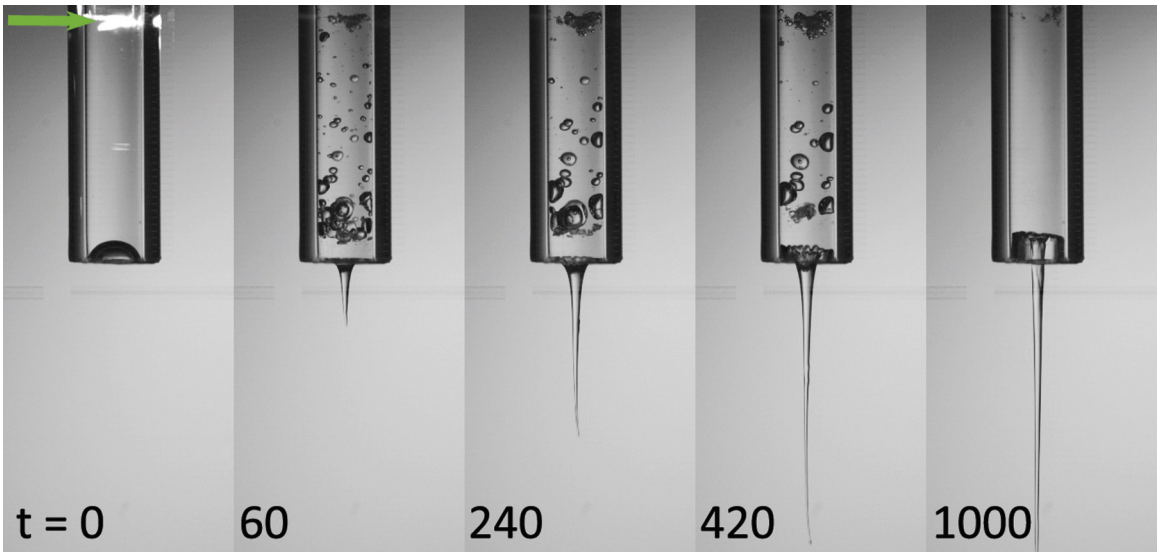

Fig. 7 – Select frames from a high-speed video sequence of the laser-induced jet formation process for water in a 2.7 mm inner diameter capillary. The jet speed is 46 m/s. The time in each frame is in microseconds. The bright spot in the tube in the first image is a manifestation of the plasma created by the focused laser pulse.

(measured at the bottom of the field-of-view) is 380 μm. This particular realization, whilst dramatically different from that shown in Fig. 4, exhibits the ability of the system to self-correct and form a steady stream within a few milliseconds. The difference in the jet diameters is discussed in Section 3.2.

In contrast, Fig. 6 presents an example whereby a small volume of water is attached to the exterior of the tip of the cartridge. In this case, again, the system is capable of "clearing" the defect within a few milliseconds, however, we observe a pronounced deflection (and dispersion) of the jet in the direction of the original location of the water droplet on the tip. This is akin to the well-known *teapot effect*, describing jet and sheet deflections upon leaving an orifice or substrate. Note that the realizations shown in Figs. 5 and 6 do indicate a dependence on initial conditions, however, they also indicate that the system is capable of reaching a steady jet formation for injection purposes regardless.

In contrast to the plunger-based method where fluid is force out of a fixed orifice, we now present two qualitative examples, in Figs. 7 and 8 of the laser-induced jet formation. Here, the jet is the product of the pressure pulse interaction with the concave meniscus. In Fig. 7, the green arrow in the first image indicates the direction of the laser pulse from the left, whilst the bright white region is an optical manifestation of the plasma created by the focused laser pulse (Philipp and Lauterborn, 1998). The subsequent frames taken at $t = 60$, 240, 420 and 1000 μs show the emergence of a tapered jet, with an effective jet velocity of $V_{jet} \approx 46$ m/s. Cavitation bubbles are observed inside the tube due to the shock wave propagation through the liquid. It is this shock wave which interacts with the concave meniscus to produce the jet (Tagawa et al., 2012, 2013; Gonzalez Avila et al., 2015). Fig. 8 shows a close-up view of the jet start-up phase for this process. Note the initial flattening of the meniscus at $t = 50$ μs and the distinctive tapered

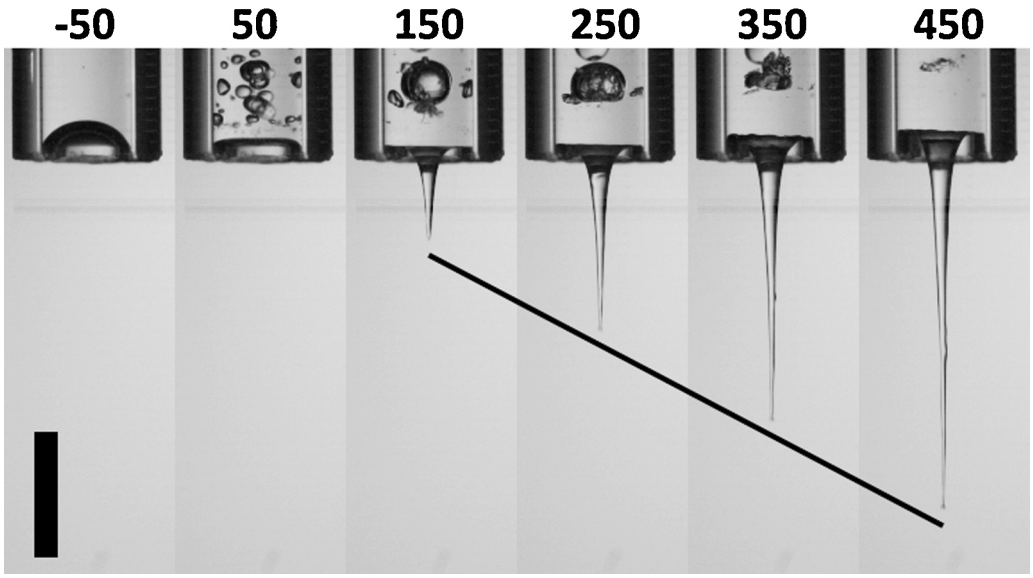

Fig. 8 – Frames from a high-speed video sequence of the start-up phase for a laser-induced jet device with orifice diameter 2.4 mm. The times displayed above the images are in microseconds. The scale bar is 5 mm long. The black diagonal line indicates a linear motion of the jet tip.

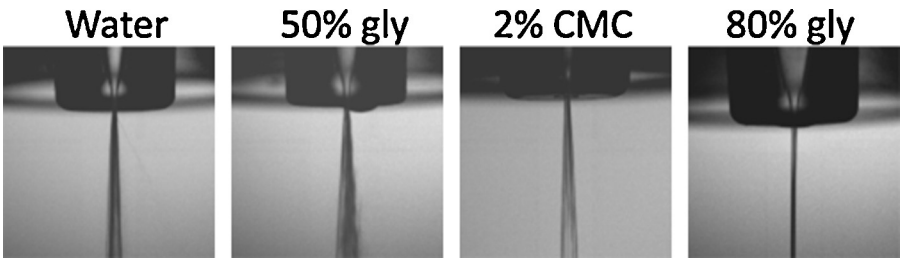

Fig. 9 – Snapshots from a high-speed video recorded at 310,000 fps of fully-developed jet streams from commercial spring-actuated devices. Approximate jet Reynolds numbers are $Re \approx 15$, 280, 1820, 310 and 154 based on the orifice diameter of 157 μm.

appearance of the jet at later times. The jet velocity in this realization is $V_{jet} = 35.9$ m/s, with a jet diameter from 165 μm at the tip to approximately 1 mm near the orifice.

The expansion of the cavitation bubbles inside the tube may influence the expelled volume of liquid, but appear to have little influence on the jet structure. The lower jet speeds and smaller volumes ejected with this technique render single jet injection impractical, however multiple pulses could be used to deliver higher volumes (Kato et al., 2014; Arora et al., 2007). One potential adverse affect could be the interaction of the cavitation bubbles with drug molecules in the liquids to be delivered in real applications, given that the temperature associated with bubble collapse can reach 15,000 K (Lohse et al., 2005).

3.2. *Steady stream spread versus tapering*

Successful drug deposition is dependent upon maintaining the integrity of the jet, thus atomization and formation of spray droplets is undesirable (e.g. Figs. 5 and 6). Further loss of drug dosage can occur through splashing at the skin and thus a streamlined jet is preferable. Fig. 9 shows examples of the most divergent steady jet streams for various fluids, clearly showing that significant jet spread can occur. This phenomenon is well-understood for turbulent jets (Wu et al., 1995; Umemura, 2014; Lin and Reitz, 1998; Schramm-Baxter and Mitragotri, 2004) due to the development of a shear layer inside the converging nozzle in the orifice and a boundary layer of the ambient fluid (air in our case) upon leaving the orifice. Thus, the difference in velocity and density between the jet and ambient air is a key factor in the observation of such jet streams.

To quantify the spread of the jet, we measure an effective spray angle (Sou et al., 2007) for different fluids, as shown in Fig. 10. The spray angle is thus given by

$$\theta = \tan^{-1}\left(\frac{D_h - D_0}{2h}\right) \quad (3)$$

For example, in Fig. 10, the effective spray angle of $\theta \approx 1.45^\circ$. Whilst this may seem small, it is important to bear in mind that an angle of just 1.45° over a stand-off distance of 1 cm will lead to an effect jet diameter at impingement of $D_{jet} \approx 660$ μm, significantly larger than the orifice diameter of $D_0 = 157$ μm.

This expanded jet cross-section will therefore have an impact on the overall jet dynamics and penetration depth. Based upon multiple (minimum of 15) repeat trials for each fluid, the mean spray angles are $\bar{\theta} = 0.74^\circ$, 0.59°, 0.43° and for water, 50% glycerol, 80% glycerol for $D_0 = 114$ μm and $\bar{\theta} = 1.15^\circ$, 1.68°, 0.51° and 0.79° for water, 50% glycerol, 80% glycerol and 2% CMC respectively for $D_0 = 157$ μm. The highest variation amongst the repeat trials was observed for the CMC solution

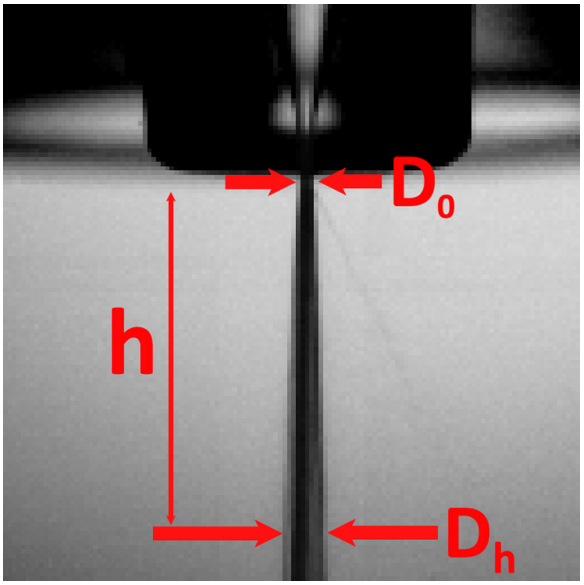

Fig. 10 – Snapshot showing the parameters measured for characterizing the spread of the jet.

and water, whilst the highest absolute value of $\bar{\theta}$ was observed with 50% glycerol, indicating that the fluid composition may play a role in maintaining the integrity and shape of the jet. Although a decreasing angle, θ, with increasing μm was observed for $D_0 = 114$ μm, further tests with a broader range of fluid properties and orifice diameters may be warranted to conclusively determine their influence on θ.

In contrast, jets produced by the laser-induced method exhibit tapering in the early stages, followed by a constant diameter toward the latter stage of the ejection, shown by the representative images in Fig. 11(a) and (b). The tapered jet stream has a tip diameter of approximately 110 μm ($D_{tip}/D_0 \approx 0.1$), whilst the jet diameter at the opening of the tube is $D_0 = 1.1$ mm. The constant diameter in Fig. 11(b) (at the end of the ejection period) is 220 μm ($D_{jet}/D_0 \approx 0.2$). Slender

Table 1 – Mean spray angles for different orifice diameters and fluid dynamic viscosities.

D_0 (μm)	μ (mPa s)	$\bar{\theta}$ (deg)
114	1	0.74
114	8	0.59
114	85	0.43
157	1	1.15
157	8	1.68
157	85	0.51
157	37[a]	0.79

[a] Note the indicates zero shear viscosity, μ_0.

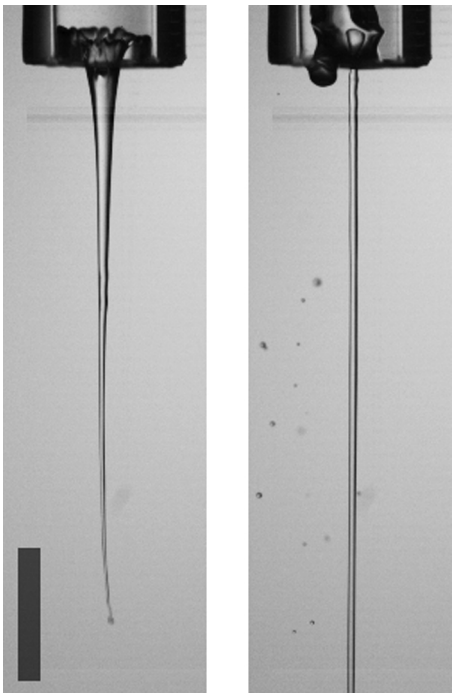

Fig. 11 – Snapshots taken at (a) $t = 500\,\mu s$ and (b) $t = 6.5$ ms from the laser pulse showing (a) tapered jet formation and (b) constant diameter jet. The scale bar is 5 mm.

jets, such as those found herein for the laser-induced method, were also reported by Tagawa et al. (2012, 2013). Note that the total duration of the ejection for the laser-induced jets is typically less than 10 ms (7 ms for the realization shown in Fig. 11), thus significantly smaller volumes are available than with the Bioject devices, where the total duration can be >100 ms depending upon the desired injection volume.

The start-up time is defined to be the time from jet actuation to the steady jet stream formation, i.e. from the very first motion from the orifice until a steady jet stream is observed for the Bioject device, whereas for the laser-induced method, we take the time from the laser pulse to the jet exit. Thus the start-up time for the laser-induced method is very short, with $t \approx 100\,\mu s$. In contrast, the start-up time for the Biojector 2000 can vary dependent upon the initial state of the orifice – for example whether any residual liquid is present on the orifice tip or bubbles in the drug reservoir. In such cases, the total start-up time can be $t \gtrsim 20$ ms. In the absence of any residual liquid, the typical start-up time is $t \approx 5$ ms, which appears to be determined by the motion of the plunger, which exhibits a rather impulsive start before attaining a steady (linear) motion, as discussed in Section 3.3.

3.3. *Jet velocity and power*

For steady jet streams, direct measurement of velocity becomes difficult due to lack of distinct tracking points. Previously, the exit velocity of the jet has been deduced by the total jet duration period (Baxter and Mitragotri, 2005). In our experiments, we track the motion of the plunger and apply mass conservation for incompressible fluids:

$$V_p D_p^2 = V_{jet} D_0^2 \tag{4}$$

where V_p is the plunger speed and $D_p = 8$ mm is the inner diameter of the cartridge. Fig. 12(a) shows example displacement–time curves for the tip of the plunger once motion has commenced. There is an initial impulsive motion for $t \lesssim 5$ ms followed by a linear displacement regime for $t \gtrsim 10$ ms, indicated by the solid trendlines. By taking the slopes of these trendlines for multiple realizations, we can deduce the average plunger speeds which, for these fluids range from $V_p \approx 2.7$ cm/s for water, $V_p = 2.4$ cm/s for 50% glycerol, and $V_p = 1.9$ cm/s for $\mu = 85$ mPa s. Based upon these plunger speeds, the mass conservation equation provides us with the exit velocities for these fluids as $V_{jet} \approx 134$ m/s, 116 m/s and 95 m/s for water, 50% glycerol and 80% glycerol respectively, shown in Fig. 12(b). The dependence of jet exit speed upon fluid viscosity is therefore relatively weak, with $V_{jet} \sim \mu^{-0.08}$, which is surprising given that the pressure drop across the orifice would be expected to follow a linear relationship with viscosity.

One convenient way to collect the relevant jet parameters, including velocity, is with the jet power (Schramm-Baxter and Mitragotri, 2004), P_{jet}, defined as the rate of change of kinetic energy, $\frac{1}{2}\dot{M}V_{jet}^2$, where $\dot{M} = \rho A V_{jet}$, giving

$$P_{jet} = \frac{1}{8}\rho\pi D^2 V_{jet}^3 \tag{5}$$

Based on the calculated jet velocities and orifice diameters used, the range of jet powers available with the Biojector devices is $P_{jet} \approx 5$–24 W, whilst laser-induced jets and other mechanisms (e.g. Kato et al., 2014; Gonzalez Avila et al., 2015) produce a significantly lower power with $P_{jet} = O(0.01$–$1)$ W for most cases. Given that it was previously found (Schramm-Baxter and Mitragotri, 2004) that the depth of penetration correlated well with the jet power, this means that the single laser-induced jets may not be suitable for a range of application where deeper sub-cutaneous or intra-muscular deposition is desired. For jets with diameters less than ~100 μm produced by pulsed laser or piezoelectric actuation (e.g. Flethcer et al., 2002; Arora et al., 2007; Tagawa et al., 2013; Gonzalez Avila et al., 2015), the penetration depth is typically of the order of 100s of microns, up to a maximum of 5 mm. However, multiple consecutive pulsed jets were able to penetrate up to 9 mm (Kato et al., 2014) in a 5% gelatin target, meaning that a pulsed system may be capable of reaching more desirable depths.

3.4. *Penetration dynamics*

Various empirical models have been proposed for the penetration dynamics and the final hole depth in jet injections. We briefly recapitulate the main approaches before presenting our observations; Baxter and Mitragotri (2005) presented a model based upon a critical stress, $\sigma_c = \frac{1}{2}\rho v_c^2$, and centerline velocity (in turbulent jet flows), $v_m = \frac{1}{2C}\frac{V_0 D_0}{x}$, where V_0 is the core jet velocity, D_0 is the nozzle orifice diameter and x is the downstream distance. By substituting in the stand-off distance, x_s so that the hole depth is $h_d = x - x_s$, then

$$h_d = \frac{V_0 D_0}{2C}\sqrt{\frac{\rho}{2\sigma_c}} - x_s \tag{6}$$

Kato et al. (2014) presented a model of penetration based on the contraction force from the gel opposing the jet. The force is comprised of both viscoelastic energy and the hydrostatic force from the weight of the gel. Since the force is higher for

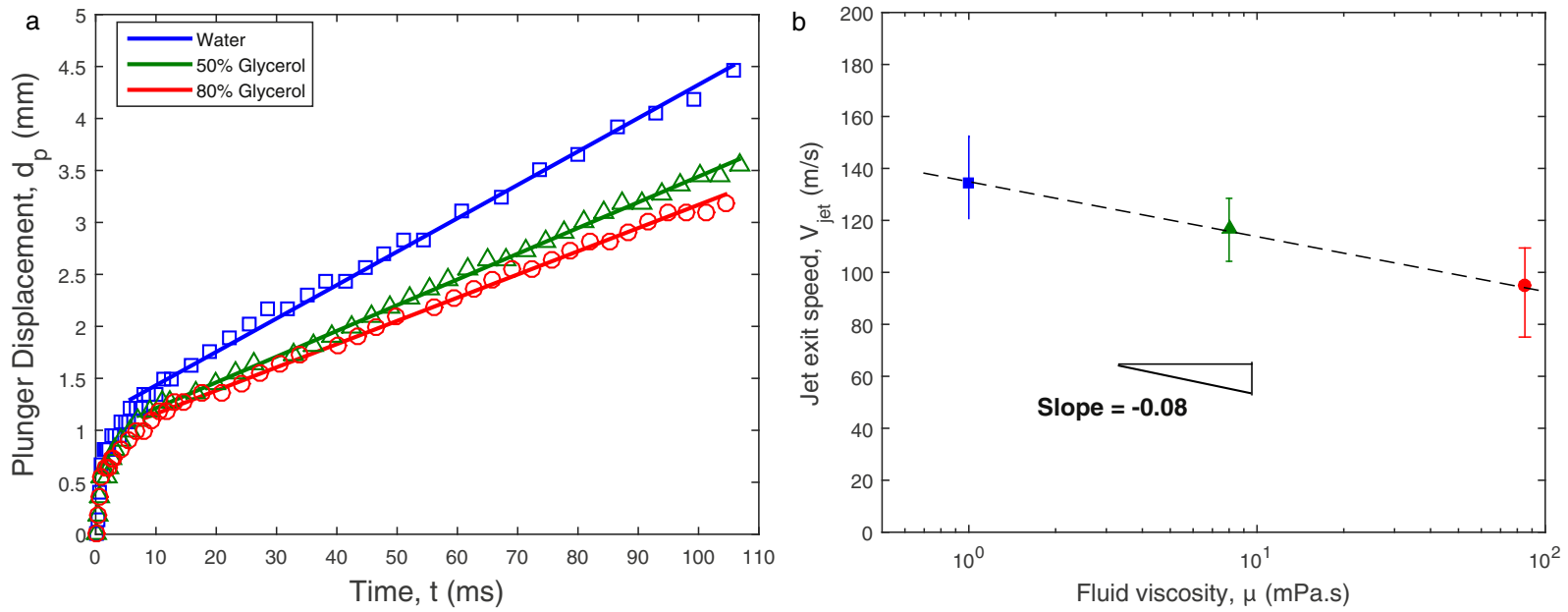

Fig. 12 – (a) Example displacement–time curves for the tip of the plunger tracked over a 100 ms interval for $D_0 = 114\,\mu m$. (b) Derived jet exit speeds, V_{jet}, showing a weak dependence on fluid viscosity, μ.

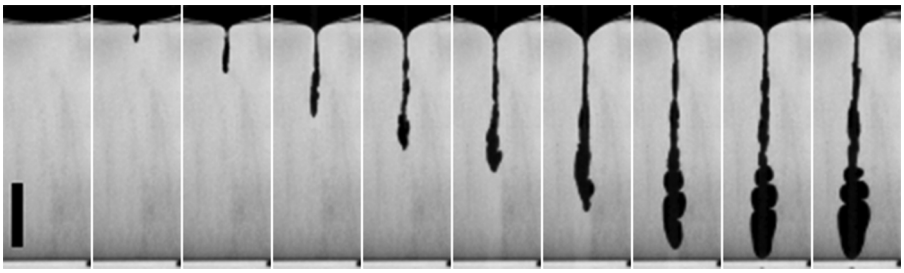

Fig. 13 – Water jet with $D_0 = 114\,\mu m$ penetrating into a gelatin target ($2\%_{w/w}$). The frames shown are taken at times $t = 0$, 0.2, 0.4, 0.6, 0.8, 1, 1.3, 1.9, 2.6 and 3.2 ms from the moment the jet first impacts the gel. The stand-off is $x_s \approx 2$ mm. The scale bar in the first image is 5 mm long.

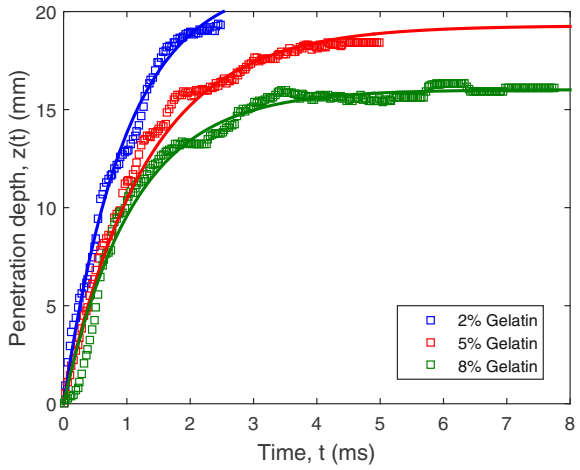

Fig. 14 – Water jet with $D_0 = 157\,\mu m$ and $V_0 = 134$ m/s penetrating into a gelatin targets ($2\%_{w/w}$, $5\%_{w/w}$ and $8\%_{w/w}$). The data points are determined by tracking the tip of the hole, whilst the solid lines are fits to Eq. (8).

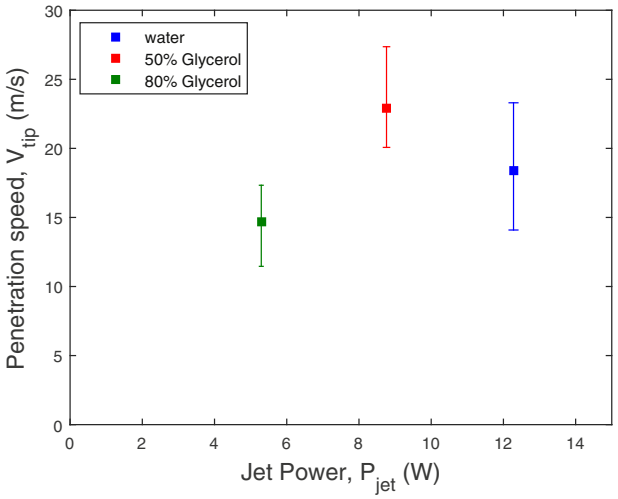

Fig. 15 – Tip speed during the linear regime ($t \lesssim 1$ ms) of gel penetration ($5\%_{w/w}$ gelatin) plotted versus the jet power, $P = \frac{1}{8}\pi\rho D_0^2 V_{jet}^3$.

deeper penetration, it is proportional to the depth and the displacement x(t) is given by

$$x(t) = [x_0 + (v_0 + \gamma x_0)t]e^{-\gamma t} \tag{7}$$

where $x_0 = x(t = 0)$ and $v_0 = v(t = 0)$ and γ is a fitting parameter with units of s^{-1}.

Lastly, Tagawa et al. (2013) presented a viscous stress model based on the stress at the wall of the hole created by the jet. This resulted in a simple model of the penetration depth as a function of time as

$$z(t) = \frac{V_{jet} - V_{crit}}{c_v}(1 - e^{-c_v t}) \tag{8}$$

where V_{crit}, a fitted parameter, is the critical speed needed to puncture the surface of the gel and c_v is a second fitting parameter with units of s^{-1}.

Fig. 13 presents an example of a water jet ($D_0 = 114\,\mu m$, $V_{jet} = 134$ m/s) deposited into a 2% gelatin target. The frames

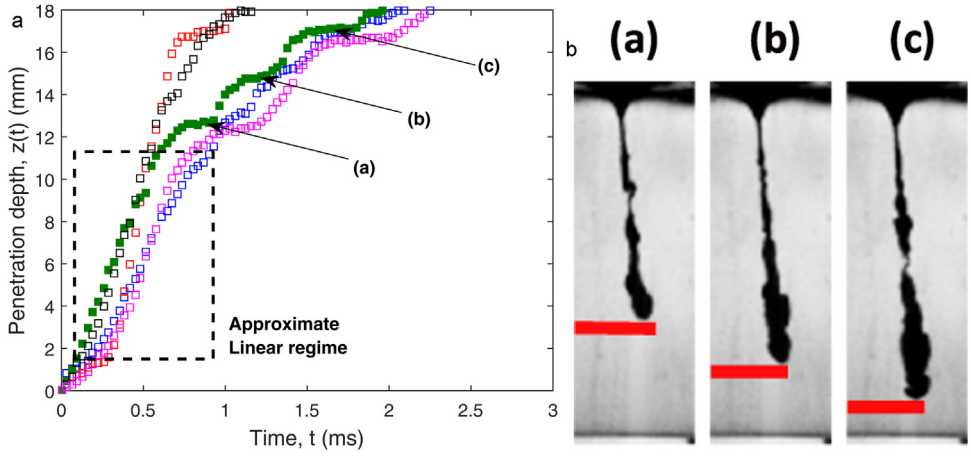

Fig. 16 – Water jet with $D_0 = 157\,\mu m$ and $V_0 = 134$ m/s penetrating into an $8\%_{w/w}$ gelatin target. Five different realizations are shown. The images to the right correspond to short-term plateaus for the green data points.

shown are representative of typical jet injections into gel substrates, showing the jet penetrating rapidly over the first millisecond, then slowing as fluid accumulation occurs, with distinct bulbous regions forming. Given the high contrast in the video sequences, tracking the tip of the hole becomes straightforward and we can thus extract the penetration depth as a function of time. One example, highlighting the influence of the target substrate is shown in Fig. 14, where three realizations of a water jet ($P = 23.2$ W) deposited into different weights of gelatin are presented.

The initial penetration stage ($t \lesssim 1$ ms) exhibits a near-linear penetration regime in time (i.e. constant velocity regime), but a plateau at later times. The overall displacement–time curves are best described by an exponential decay, based upon the viscous stress model (8). Example fits to this equation are shown in Fig. 14. In these fits, we observe critical speeds of $V_{crit} \approx 110$ m/s and $c_v = O(10^3)$. The final penetration depths observed in these data sets are approximately 16, 18.4 and 19.3 mm.

During the initial penetration stage, the data exhibits very little dependence on the viscosity of the jet fluid or the jet power, as demonstrated by the data in Fig. 15. From all of our data across multiple trials for different fluids, we did not observe a quantifiable trend for the early-time penetration speed in terms of the fluid properties or the jet power, but in general the tip of the jet penetrates with a speed of $V_{tip} \approx 12 - -27$ m/s. Therefore, more jet fluids should be tested with both homogeneous and heterogeneous targets.

Whilst Eq. (8) can provide reasonable fits to our data, we caution that it may not be applicable across the entire evolution in most cases due to the longer injection times with the Biojector 2000 device compared to the laser-induced method (Tagawa et al., 2013; Kato et al., 2014). For longer injection periods, interaction between the target and the incoming

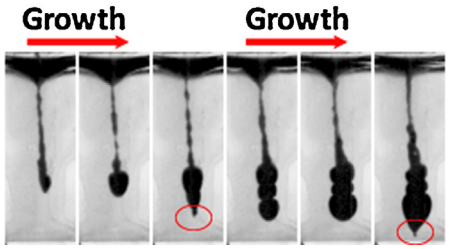

Fig. 17 – Image sequence showing the growth of reservoirs in the gel and sudden puncturing (red circles) followed by a short penetration stage to the next reservoir depth. The jet fluid is 80% glycerol and the gel is 8%$_{w/w}$ gelatin. Frames shown are taken at times t = 0.99, 2.68, 4.37, 7.05, 10.73 and 11.13 ms from when the jet first hits the target. (For interpretation of the references to color in this figure legend, the reader is referred to the web version of the article.)

jet stream becomes increasingly significant. In particular, we observe the formation of miniature reservoirs, manifested by short-term plateaus in the penetration depth. An example of this feature is highlighted by the data in Fig. 16. These plateaus typically develop for $z > 12$ mm and physically correspond to the formation of bulbous regions at the tip, shown by images (a), (b) and (c), respectively. Fig. 17 provides a clear example of the discrete growth and penetration stages for an 80% glycerol jet in an 8%$_{w/w}$ gelatin target. Each growth stage is followed by a sudden puncturing down to the next reservoir depth (see images 3 and 6 in the sequence).

When the incoming fluid from the jet stream enters the reservoir, it encounters back-flow and circulation and potentially high pressure caused by the local contraction of the gel due to elastic stress. Eventually, the incoming jet stream reaches the tip of the hole in the gel and punctures the gel

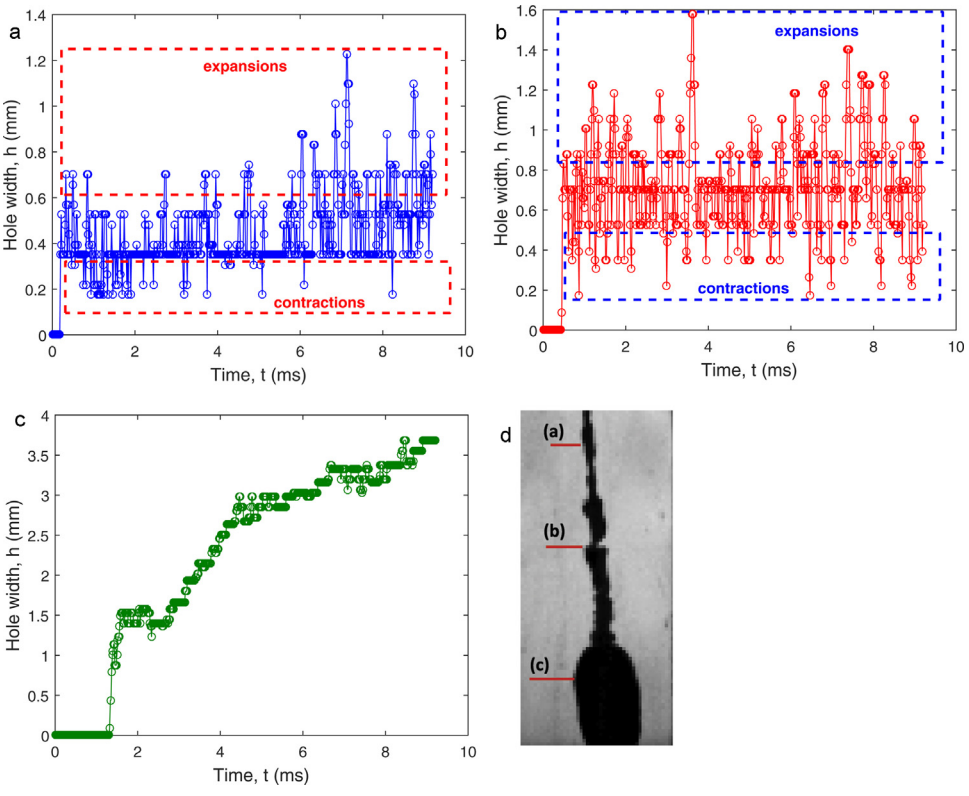

Fig. 18 – Hole width versus time for three depths (a) $d_p = 3.9$ mm, (b) $d_p = 9.3$ mm and (c) $d_p = 16.4$ mm below the surface of the gel. The image to the right shows the depths analyzed on an image taken 7 ms after the jet first contacts the gel.

to allow further penetration. The data thus exhibits step-like displacements after the linear regime where the elastic properties of the gel must be incorporated to correctly describe the dynamics. This suggests that the model of Kato et al. (2014) may be adapted to longer-duration single injections to provide an adequate description of the step-wise penetration.

To further support the notion that elastic stress should be incorporated, we present evidence of continual expansion-contraction of the hole along the entire depth; Fig. 18 shows the hole width versus time for three set depths ((a) $z = 3.5$, (b) $z = 8.7$ and (c) $z = 15.7$ mm) below the gel surface. The image to the right shows a snapshot of the process at $t = 7.9$ ms from the start of injection marked with the depths where the data is taken. In Fig. 18(a), the modal hole width is 350 μm, however, there is considerable fluctuation around this width, corresponding to short expansions and contractions resulting from competition between the inertial pressure from the incoming jet stream ($\sim\rho V_{jet}^2$) and the elastic stress (σ) in the surrounding gel. Deeper in the gel, Fig. 18(b) indicates a modal width of 708 μm with more significant fluctuations between 0.2 and 1.6 mm. Lastly, in Fig. 18(c), for $Z = 15.7$ mm, the expansion-contraction regime does not occur, rather we observe a more steady growth representing the gradual expansion of the main fluid reservoir. The sharp fluctuations in the hole width indicate that the hole at some points becomes comparable to the initial jet diameter (possibly smaller given the stream spread calculated in Section 3.2). This constant interplay between the incoming fluid and the target must therefore be taken into account to accurately describe the penetration dynamics.

In summary, jet penetration into soft tissues is a complex phenomenon. The jet must be powerful enough to first puncture the surface, then provide sufficient inertia to overcome both elastic and hydrodynamic stress in order to penetrate. The yield strength of the target could be determined by the critical stress required to puncture the surface by careful adjustment of jet speed, $\sigma_c \sim \frac{1}{2}\rho V_{jet,*}^2$ (e.g. Tagawa et al., 2013 found a critical jet speed of approximately 20 m/s in order to puncture a 5%$_{w/w}$ gelatin target), whilst estimates of the elastic and hydrodynamic stress in the bulk can be deduced by the inertial pressure at the tip during penetration, $\sim\frac{1}{2}\rho V_{tip}^2 \approx O(10^5)$ Pa. However, our detailed visualization indicates that there is an intricate interplay between the incoming fluid jet and the target substrate. In particular, elasticity appears to play an important role in the penetration and formation of fluid reservoirs. Given that using homogeneous gels may not be entirely representative of true injections due to the heterogeneous structure of both cutaneous and sub-cutaneous material, it is therefore recommended to investigate a broader range of heterogeneous materials coupled with both particle-laden and higher-viscosity fluids.

4. Conclusions

A study of jet formation for needle-free injection was performed with the aid of high-speed videography. Various characteristics such as the jet start-up time, steady stream divergence and speed were deduced for both a pressure-driven plunger device and a laser-induced cavitation device. Whilst a more streamlined (tapered) jet was observed in most cases for the laser-induced method, a comparison with commercial devices show that the significantly lower jet power may not be able to achieve the penetration depths that are available with current marketed technology. Our experiments revealed that the jet speed is very weakly inversely correlated with the fluid viscosity, $V_{jet} \sim \mu^{-0.08}$, however, this dependence needs to explored over a broader parameter regime, incorporating more high-viscosity and non-Newtonian fluids.

Penetration into homogeneous gels was analyzed and different regimes were observed. In particular, the Bioject devices with $P = O(20)$ W displayed a linear penetration regime for $t \lesssim 1$ ms followed, in some cases, by a step-like penetration in time due to the formation of miniature reservoirs at depths of approximately 1–2 cm. A more comprehensive model of jet injection should account for this phenomenon. We did not identify any dependence of the penetration on jet fluid properties, which could be an indication that penetration is dictated by the material properties of the target medium such as stiffness or elastic modulus. However, this needs to be verified. It would also be constructive to assess the effects of interfacial tension between the jet and the substrate.

In contrast, laser-induced and other short pulsejets only penetrate up to a maximum of a few millimeters below the surface of different gels. Specific to the laser-induced method, the interaction of cavitation bubbles and high temperatures with molecules in the medicinal products is an aspect that needs to be evaluated in more detail.

It has been proposed (Arora et al., 2007) that pain and bruising associated with deeper needle-free injections may be due to the interaction of the liquid jet with blood vessels and tissue. Whilst shallow penetrations have been achieved (e.g. Park et al., 2012; Kato et al., 2014; Arora et al., 2007, 2008; Stachowiak et al., 2007, 2009; Tagawa et al., 2013; Gonzalez Avila et al., 2015), the deposited volumes are significantly lower than those available with commercial devices. Thus mechanisms targeting shallow deposition *and* larger volumes should be sought. In order to expand upon current capabilities, a more extensive parameter space should be explored, especially in terms of jet fluid properties by considering non-Newtonian and polymeric fluids. Such work is currently underway.

References

Apitz, I., Vogel, A., 2005. Material ejection in nanosecond Er:YAG laser ablation of water, liver, and skin. Appl. Phys. A 81, 329.

Arora, A., Hakim, I., Rathnasingham, Srinivasan, R., Fletcher, D.A., Mitragotri, S., 2007. Needle-free delivery of macromolecules across the skin by nanoliter-volume pulsed microjets. PNAS 104, 4255–4260.

Arora, A., Prausnitz, M.R., Mitragotri, S., 2008. Micro-scale devices for transdermal drug delivery. Int. J. Pharm. 364, 227–236.

Baxter, J., Mitragotri, S., 2005. Jet-induced skin puncture and its impact on needle-free jet injections: experimental studies and a predictive model. J. Control. Release 106, 361–373.

Chen, R.C.C., Yu, Y.T., Su, K.W., Chen, Y.F., 2013a. Exploring morphological variations of a laser-induced water jet in temporal evolution: formation of an air bubble enclosing a water drop. Laser Phys. 23, 116002.

Chen, R.C.C., Yu, Y.T., Su, K.W., Chen, J.F., Chen, Y.F., 2013b. Exploration of water jet generated by Q-switched laser induced water breakdown with different depths beneath a flat free surface. Opt. Express 21, 445–453.

Darling, C.L., Maffei, M.E., Fried, W.A., Fried, D., 2008. Near-IR imaging of Erbium laser ablation with a water spray. Proc. Soc. Photo Opt. Instrum. Eng. 20, 6843.

Flethcer, D., Palanker, D.V., Huie, P., Miller, J., Marmor, M.F., Blumenkranz, M.S., 2002. Intravacular drug deliver with a pulsed liquid microjet. Arch. Ophthalmol. 120, 1206–1208.

Frenz, M., Romana, V., Zweig, A.D., Weber, H.P., Chapliev, N.I., Silenok, A.V., 1989. Instabilities in laser cutting of soft media. J. Appl. Phys. 66, 4496.

Frenz, M., Paltauf, G., Schmidt-Kloiber, H., 1996. Laser-generated cavitation in absorbing liquid induced by acoustic diffraction. Phys. Rev. Lett. 76, 3456–3459.
Gonzalez Avila, S.R., Song, C., Ohl, C.-D., 2015. Fast transient microjets induced by hemispherical cavitation bubbles. J. Fluid Mech. 767, 31–51.
Gregorcic, P., Diaci, J., Mozina, J., 2013. Two-dimensional measurements of laser-induced breakdown in air by high-speed two-frame shadowgraphy. Appl. Phys. A 112, 49–55.
Heijnen, L., Quinto-Su, P.A., Zhao, X., Ohl, C.-D., 2009. Cavitation within a droplet. Phys. Fluids 12, 091102.
Kale, T.R., Momin, M., 2014. Needle free injection technology – an overview. Innov. Pharm. 5, 148.
Kato, T., Arafune, T., Washio, T., Nakagawa, A., Ogawa, Y., Tominaga, T., Sakuma, I., Kobayashi, E., 2014. Mechanics of the injected pulsejet into gelatin gel and evaluation of the effect by puncture and crack generation and growth. J. Appl. Phys. 116, 074901.
Kendall, M., Mitchell, T., Wrighton-Smith, P., 2004a. Intradermal ballistic delivery of micro-particles into excised human skin for pharmaceutical applications. J. Biomech. 37, 1733–1741.
Kendall, M.A.F., Quinlan, N.J., Thorpe, S.J., Ainsworth, R.W., Bellhouse, B.J., 2004b. Measurements of the gas and particle flow within converging–diverging nozzle for high speed powered vaccine and drug delivery. Exp. Fluids 37, 128–136.
Li, Z.G., Liu, A.Q., Klaseboer, E., Zhang, J.B., Ohl, C.-D., 2013. Single cell membrane poration by bubble-induced microjets in a microfluidic chip. Lab Chip 6, 1144–1150.
Lin, S.P., Reitz, R.D., 1998. Drop and spray formation from a liquid jet. Annu. Rev. Fluid Mech. 30, 85–105.
Lindau, O., Lauterborn, W., 2003. Cinematographic observation of the collapse and rebound of a laser-produced cavitation bubble near a wall. J. Fluid Mech. 479, 327–348.
Lindinger, A., Hagen, J., Socaciu, L.D., Bernhardt, T.M., Woste, L., Duft, D., Leisner, T., 2004. Time-resolved explosion dynamics of H_2O droplets induced by femtosecond laser pulses. Appl. Opt. 43, 5263.
Lohse, D., 2005. Cavitation hots up. Nature 434, 33–34.
Marston, J.O., Thoroddsen, S.T., 2015. Laser-induced micro-jetting from armored droplets. Exp. Fluids 56, 140.
Michinaka, Y., Mitragotri, S., 2011. Delivery of polymeric particles into skin using needle-free liquid jet injectors. J. Control. Release 153, 249–254.
Mitragotri, S., 2006. Current status and future prospects of needle-free liquid jet injectors. Nat. Rev. Drug Discov. 5, 543–548.
Musapelo, T., Murray, K.K., 2014. Particle formation by infrared laser ablation of MALDI matrix compounds. J. Mass Spectrom. 49, 543–549.
Park, M-A., Jang, H-J., Sirotkin, F.V., Yoh, J.J., 2012. Er:YAG laser pulse for small-dose splashback-free microjet transdermal drug delivery. Opt. Lett. 37, 3894–3896.
Philipp, A., Lauterborn, W., 1998. Cavitation erosion by single laser-produced bubbles. J. Fluid Mech. 361, 75–116.
Pohl, R., Visser, C.W., Romer, G.R.B.E., Sun, C., Huis in't Veld, A.J., Lohse, D., 2014. High-resolution imaging of ejection dynamics in laser-induced forward transfer. Proc. SPIE 8967, 89670X.
Schramm-Baxter, J., Mitragotri, S., 2004. Needle-free jet injections: dependence of jet penetration and dispersion in the skin on jet power. J. Control. Release 97, 527–535.
Shrestha, B., Nemes, P., Vertes, A., 2010. Ablation and analysis of small cell populations and single cells by consecutive laser pulses. Appl. Phys. A 101, 121–126.
Sou, A., Hosokawa, S., Tomiyama, A., 2007. Effects of cavitation in a nozzle on liquid jet atomization. Int. J. Heat Mass Transf. 50, 3575–3582.
Stachowiak, J.C., von Muhlen, M.G., Li, T.H., Jalilian, L., Parekh, S.H., Fletcher, D.A., 2007. Piezoelectric control of needle-free transdermal drug delivery. J. Control. Release 124, 88–97.
Stachowiak, J.C., Li, T.H., Arora, A., Mitragotri, S., Fletcher, D.A., 2009. Dynamic control of needle-free jet injection. J. Control. Release 135, 104–112.
Stolee, J., Vertes, A., 2013. Toward single-cell analysis by plume collimation in laser ablation electrospray ionization mass spectrometry. Anal. Chem. 85, 3592–3598.
Stout, R. Personal communication with Bioject CMO.
Taberner, A., Hogan, N.C., Hunter, I.W., 2012. Needle-free injection using real-time controlled linear Lorentz-force actuators. Med. Eng. Phys. 34, 1228–1235.
Tagawa, Y., Oudalov, N., Visser, C.W., Peters, I.R., van der Meer, D., Sun, C., Prosperetti, A., Lohse, D., 2012. Highly focused supersonic microjets. Phys. Rev. X 2, 031002.
Tagawa, Y., Oudalov, N., El Ghalbzouri, A., Sun, C., Lohse, D., 2013. Needle-free injection into skin and soft matter with highly focused microjets. Lab Chip 13, 1357–1363.
Thoroddsen, S.T., Takehara, K., Etoh, T.G., Ohl, C.-D., 2009. Spray and microjets produced by focusing a laser pulse into a hemispherical drop. Phys. Fluids 21, 112101.
Umemura, A., 2014. Model for the initiation of atomization in a high-speed laminar liquid jet. J. Fluid Mech. 757, 665–700.
Vogel, A., Horneffer, V., Lorenz, K., Linz, N., Huttmann, G., Gebert, A., 2007. Principles of laser microdissection and catapulting of histologic specimens and live cells. Laser Manip. Cells Tissues 82, 153–205.
Wu, P.-K., Miranda, R.F., Faeth, G.M., 1995. Effect of initial flow conditions on primary breakup of nonturbulent and turbulent round liquids jets. Atomiz. Sprays 5, 175–196.
Zhiyuan, Z., Hua, G., Zhenjun, F., Jie, X., 2014. Characteristics of droplets ejected from liquid propellants ablated by laser pulses in laser plasma propulsion. Plasma Sci. Technol. 16, 251–254.
Zhu, L., Gamez, G., Schmitz, T.A., Krumeich, F., Zenobi, R., 2010. Material ejection and redeposition following atmospheric pressure near-field ablation on molecular solids. Anal. Bioanal. Chem. 396, 163–172.